International Journal of Heat and Fluid Flow 30 (2009) 32–43

Contents lists available at ScienceDirect

International Journal of Heat and Fluid Flow

journal homepage: www.elsevier.com/locate/ijhff

Detached eddy simulation of cyclic large scale fluctuations in a simplified engine setup

Christian Hasse *, Volker Sohm [1], Bodo Durst

BMW Group, EA, Powertrain Development, 80788 München, Germany

ARTICLE INFO

Article history:
Received 25 February 2008
Received in revised form 2 September 2008
Accepted 4 October 2008
Available online 28 November 2008

Keywords:
SST DES
Cyclic variations
Engines
Hybrid RANS/LES
Tumble

ABSTRACT

Computational Fluid Dynamics using RANS-based modelling approaches have become an important tool in the internal combustion engine development and optimization process. However, these models cannot resolve cycle to cycle variations, which are an important aspect in the design of new combustion systems. In this study the feasibility of using a Detached Eddy Simulation (DES) SST model, which is a hybrid RANS/LES model, to predict cycle to cycle variations is investigated. In the near wall region or in regions where the grid resolution is not sufficiently fine to resolve smaller structures, the two-equation RANS SST model is used. In the other regions with higher grid resolution an LES model is applied. The case considered is a geometrically simplified engine, for which detailed experimental data for the ensemble averaged and single cycle velocity field are available from Boreé et al. [Boreé, J., Maurel, S., Bazile, R., 2002. Disruption of a compressed vortex, Physics of Fluids 14 (7), 2543–2556]. The fluid flow shows a strong tumbling motion, which is a major characteristic for modern turbo-charged, direct-injection gasoline engines. The general flow structure is analyzed first and the extent of the LES region and the amount of resolved fluctuations are discussed. Multiple consecutive cycles are computed and turbulent statistics of DES SST, URANS and the measured velocity field are compared for different piston positions. Cycle to cycle variations of the velocity field are analyzed for both computation and experiment with a special emphasis on the useability of the DES SST model to predict cyclic variations.

1. Introduction

Cyclic variations of the combustion process are an important issue in engine development. Engine parameters such as the optimal spark timing are set according to the mean cycle. Consequently, fast burning cycles have overadvanced spark timing while in cycles with a slower combustion process the timing is retarded and the efficiency potential is not fully used. Additionally, since the extreme engine cycles determine the operating range of the engine, the equivalence ratio, the valve and the spark timing as well as the compression ratio are a compromise. The fast burning cycles limit the compression ratio and the engine's fuel octane requirement due to the tendency to knock and the slower burning cycles define the lean operation limit and the amount of EGR that can be applied.

In addition to the above mentioned limitations in DI engines with stratified combustion modes cycle to cycle variations can play an important role since these variations may cause a decisive influence whether the condition (gas motion and composition) in the combustion chamber and especially in the spark plug region are favorable for stable ignition and flame propagation or not. For very lean or very rich mixtures the cyclic combustion variations increase and eventually the burning rate in some cycles is so slow that the combustion process is incomplete. At a certain point even misfire can occur. The mixture fails to ignite or the flame is quenched directly after ignition, which is undesirable in terms of engine roughness, efficiency and unburned hydrocarbon emissions. This condition is significantly influenced by the flow generated during the intake process. This flow structure can be different from cycle to cycle and consequently leads to combustion variations.

During the design and optimization process of internal combustion (IC)-engines Computational fluid dynamics (CFD) using RANS turbulence modelling has proven to be a computationally efficient tool. However, this approach is limited when it comes to unsteady features as cycle to cycle variations and cannot capture this kind of phenomenon. On the other hand, LES should provide in general the ability to predict cyclic variations because smaller spatial scales and temporal fluctuations can be resolved. In LES a significantly smaller range of turbulent length scales needs to be modelled compared to the RANS approach. However, resolving smaller temporal and spatial scales requires higher order numerical schemes,

---

* Corresponding author. Tel.: +49 89 382 10375; fax: +49 89 382 70 10375.
E-mail address: Christian.Hasse@bmw.de (C. Hasse).

[1] Previously BMW Group, now Robert Bosch GmbH, Stuttgart, Germany.

0142-727X/$ - see front matter © 2008 Elsevier Inc. All rights reserved.
doi:10.1016/j.ijheatfluidflow.2008.10.001

smaller time steps and higher resolutions of the computational grids.

For wall-bounded turbulent flows at high Reynolds number in complex geometries hybrid RANS/LES approaches have become an attractive alternative to pure LES. They combine attractive features of both methods providing the opportunity to use LES in regions such as free shear layers, where its performance is superior to RANS. In other regions, where the accuracy and the averaged information on turbulent properties is sufficient, RANS can be used in order to save CPU-time. In contrast to pure RANS, it is expected that temporal fluctuations can be resolved in the LES regions giving this approach the potential to predict cycle to cycle variations, which is here investigated for the turbulent gas motion in a simplified engine setup. Detached Eddy Simulation (DES) was originally proposed by Spalart et al. (1997). Results and discussions on further model development are reported in the literature, see e.g. Travin et al. (2000, 2002); Constantinescu and Squires (2003); Yan et al. (2005); Spalart et al. (2006). Travin et al. (2002) proposed a DES variant based on the SST model by Menter (1993) and this DES SST model is used in this study.

A brief overview of the SST-based DES and URANS approaches and their implementation in the CFX solver, which is used in this study, is given in Section 2. Numerical aspects, which are of interest especially for the hybrid model, are presented in Section 3 with an emphasis on the numerical dissipation of the spatial scheme. The results for the geometrically simplified engine setup are presented in Section 4. The fluid flow is investigated for multiple consecutive cycles. The results obtained with the SST DES approach are compared to SST URANS computations and optical measurements in terms of accuracy and level of additional information.

2. Governing equations and turbulence modelling

The formulation of the filtered governing equations for mass, momentum and total enthalpy used in the CFD solver CFX are given in Eqs. (1)–(3), where $\bar{f}$ denotes a non-density-weighted filtered variable and $\tilde{f}$ is the density-weighted filtered variable, respectively

$$\frac{\partial \bar{\rho}}{\partial t} + \frac{\partial}{\partial x_i}(\bar{\rho}\tilde{u}_i) = 0, \tag{1}$$

$$\frac{\partial(\bar{\rho}\tilde{u}_j)}{\partial t} + \frac{\partial}{\partial x_i}(\bar{\rho}\tilde{u}_i\tilde{u}_j) = -\frac{\partial \bar{p}}{\partial x_j} + \frac{\partial \bar{\tau}_{ij}}{\partial x_i} - \frac{\partial \tau_{ij}^{res}}{\partial x_i}. \tag{2}$$

The equation for the total enthalpy $H = h + 0.5u_i^2$ is formulated as

$$\frac{\partial(\bar{\rho}\widetilde{H})}{\partial t} + \frac{\partial}{\partial x_i}(\bar{\rho}\tilde{u}_i\widetilde{H}) = \frac{\partial \bar{p}}{\partial t} - \frac{\partial}{\partial x_i}(\bar{q}_i + q_i^{res}) - \frac{\partial}{\partial x_i}\left[\underbrace{\tilde{u}_j(\bar{\tau}_{ij} + \bar{\rho}\widetilde{u_i''u_j''})}_{\text{viscous work}} + \underbrace{0.5\bar{\rho}\widetilde{u_i''u_j''u_j''} + \overline{u_j''\tau_{ij}}}_{\text{additional terms}}\right], \tag{3}$$

where q_i is the molecular heat flux. Due to the low mach number of the investigated flow in this study, the contributions of the viscous work as well as the additional terms are neglected. τ_{ij}^{res} and q_i^{res} are the residual momentum and heat fluxes, respectively, which require modelling

$$\tau_{ij}^{res} = \bar{\rho}(\widetilde{u_i u_j} - \tilde{u}_i\tilde{u}_j), \tag{4}$$

$$q_i^{res} = \bar{\rho}(\widetilde{u_i h} - \tilde{u}_i\tilde{h}). \tag{5}$$

This system is complemented by the filtered equation of state for perfect gases given in Eq. (6)

$$\bar{p} = \bar{\rho}\frac{R}{W}\widetilde{T}. \tag{6}$$

2.1. SST URANS Model

The model closures in this study are based on the idea by Boussinesq (1877), which reads for τ_{ij}^{res}

$$-\tau_{ij}^{res} = \mu_t\left(\frac{\partial \tilde{u}_i}{\partial x_j} + \frac{\partial \tilde{u}_j}{\partial x_i}\right) - \frac{2}{3}\delta_{ij}\left(\bar{\rho}k + \mu_t\frac{\partial \tilde{u}_k}{\partial x_k}\right), \tag{7}$$

where k is the turbulent kinetic energy. An equivalent formulation is used for the turbulent heat flux q_i^{res}.

In the context of RANS and URANS modelling, there exist a great variety of models for the turbulent viscosity. Menter (1993) proposed the shear-stress transport (SST) model, which combines the $k-\varepsilon$ by Jones and Launder (1972); Launder and Sharma (1974) with the $k-\omega$ model by Wilcox (1993). The SST model equals the standard $k-\omega$ model within the boundary layer and gradually changes to the standard $k-\varepsilon$ model in the outer region using a blending function F_1, which is described below. Besides differences in modelling constants, the transport equation for the turbulent kinetic energy given in Eq. (8) is equivalent for either the $k-\omega$ and the $k-\varepsilon$ model

$$\frac{\partial \bar{\rho}k}{\partial t} + \frac{\partial}{\partial x_i}(\bar{\rho}\tilde{u}_i k) = \widetilde{P}_k + \frac{\partial}{\partial x_i}\left[\left(\mu + \frac{\mu_t}{\sigma_k}\right)\frac{\partial k}{\partial x_i}\right] - \beta^*\bar{\rho}\omega k, \tag{8}$$

with

$$\widetilde{P}_k = min\left[\mu_t\left(\frac{\partial \tilde{u}_i}{\partial x_j} + \frac{\partial \tilde{u}_j}{\partial x_i} - \frac{2}{3}\frac{\partial \tilde{u}_k}{\partial x_k}\delta_{ij}\right)\frac{\partial \tilde{u}_i}{\partial x_j} - \frac{2}{3}\bar{\rho}k\frac{\partial \tilde{u}_k}{\partial x_k}, 10\cdot\bar{\rho}\beta^* k\omega\right]. \tag{9}$$

The terms on the r.h.s. describe the turbulent production $\widetilde{P}_k$, the turbulent diffusion and the turbulent dissipation of turbulent kinetic energy k, respectively. In order to perform the blending of the two models with one set of equations, the $k-\varepsilon$ model has been transferred into a $k-\omega$ formulation with a transport equation for ω using the simple relation $\omega = \varepsilon/(\beta^* k)$. Besides different values of modelling constants, the ω equation derived from the $k-\varepsilon$ model differs from the original $k-\omega$ model formulation by an additional cross-diffusion term, which is the last term on the r.h.s. in the following equation:

$$\frac{\partial \bar{\rho}\omega}{\partial t} + \frac{\partial}{\partial x_i}(\bar{\rho}\tilde{u}_i\omega) = \alpha\frac{\omega}{k}\widetilde{P}_k + \frac{\partial}{\partial x_i}\left[\left(\mu + \frac{\mu_t}{\sigma_\omega}\right)\frac{\partial \omega}{\partial x_i}\right] - \beta\bar{\rho}\omega^2 + 2(1-F_1)\frac{\bar{\rho}}{\sigma_{\omega 2}\omega}\frac{\partial k}{\partial x_i}\frac{\partial \omega}{\partial x_i}, \tag{10}$$

where F_1 denotes the first blending function of the SST model. It is close to 1 in the boundary layer to preserve the desirable features of the $k-\omega$ model and goes to 0 at the edge of the boundary layer to take advantage of the freestream independence of the $k-\varepsilon$ model

$$F_1 = tanh\left[\left[min\left[max\left(\frac{\sqrt{k}}{\beta^*\omega L_{wall}}, \frac{500\nu}{L_{wall}^2\omega}\right), \frac{4\bar{\rho}k}{CD_{k\omega}\sigma_{\omega 2}L_{wall}^2}\right]\right]^4\right] \tag{11}$$

with

$$CD_{k\omega} = max\left(2\bar{\rho}\frac{1}{\sigma_{\omega 2}\omega}\frac{\partial k}{\partial x_i}\frac{\partial \omega}{\partial x_i}, 10^{-10}\right). \tag{12}$$

In addition to the cross-diffusion term in the ω-equation also the model constants ζ are blended according to $\zeta = \zeta_1 F_1 + \zeta_2(1-F_1)$. Index 1 denotes the constants of the $k-\omega$ model and index 2 stands for the $k-\varepsilon$ model constants. All values are given in Table 1.

The formulation of the second blending function F_2 is very similar to the first one but extends further out into the boundary layer:

Table 1
Constants for the SST model.

β^*	α_1	β_1	σ_{k1}	$\sigma_{\omega 1}$	α_2	β_2	σ_{k2}	$\sigma_{\omega 2}$	a_1
0.09	$\frac{5}{9}$	0.075	0.5	0.5	0.44	0.0828	1	1/0.856	0.31

$$F_2 = tanh\left[\left[max\left(\frac{2\sqrt{k}}{\beta^*\omega L_{wall}}, \frac{500\nu}{L_{wall}^2\omega}\right)\right]^2\right]. \tag{13}$$

It is used for the formulation of the turbulent viscosity

$$\nu_t = \frac{a_1 k}{max(a_1\omega, \bar{S}F_2)}, \tag{14}$$

where $\bar{S}$ is the mean strain rate.

2.2. SST DES model

The idea behind the SST DES model proposed by Travin et al. (2002) is to switch from the SST RANS model to an LES model in regions, where the turbulent length scale $l_t = \sqrt{k}/(\beta^*\omega)$ predicted by the RANS is larger than the local grid spacing. In this case, the length scale in the dissipation term in the transport equation for the turbulent kinetic energy k given in Eq. (8) is replaced by the local grid spacing Δ. The standard formulation for the SST RANS model reads

$$D^k_{\mathrm{RANS}} = \bar{\rho}\varepsilon = \bar{\rho}\beta^* k\omega = \bar{\rho}\,\frac{k^{\frac{3}{2}}}{l_t}, \tag{15}$$

which is modified for the SST DES model such that as soon as the grid resolution is sufficiently fine to resolve smaller turbulent structures than the size of turbulent length scale l_t, LES should be applied

$$D^k_{\mathrm{DES}} = \bar{\rho}\,\frac{k^{\frac{3}{2}}}{l_{\mathrm{DES}}} \text{ with } l_{\mathrm{DES}} = min(l_t, C_{\mathrm{DES}}\Delta), \tag{16}$$

where $\Delta = max(\Delta_x, \Delta_y, \Delta_z)$ in our calculations. An additional limiter is introduced in this work for the formulation of the dissipation term in order to reduce the risk of grid-induced separation

$$D^k_{\mathrm{DES}} = \bar{\rho}\beta^* k\omega \cdot F_{\mathrm{DES}} \text{ with } F_{\mathrm{DES}} = max\left(\frac{l_t}{C_{\mathrm{DES}}\Delta}(1 - F_{\mathrm{SST}}), 1\right). \tag{17}$$

Using $F_{\mathrm{SST}} = 0$ recovers the original approach given in Eq. (16), where $F_{\mathrm{SST}} = F_1$ is a more conservative approach according to Menter (2008), which is used for our simulations.

In LES mode the model reduces to a two-equation $k - \omega$ SGS model and in RANS mode the standard formulation of the SST model is recovered. The value for C_{DES} of is determined in Section 3.2.

3. Numerical considerations of hybrid RANS/LES models

Numerical accuracy and numerical dissipation are essential issues in LES. In this section, we will address especially the spatial discretisation method, which is used in combination with a second order accurate backward Euler scheme for time discretisation. First we present a hybrid spatial scheme designed for DES together with the choice of the employed discretisation schemes in Section 3.1. In Section 3.2 the determination of the constant C_{DES} is discussed. Additional test cases with the same CFD solver, e.g. quantification of the error introduced by non-stationary meshes and mesh interpolation, were performed (not shown here) to ensure its applicability for hybrid RANS/LES modelling of cyclic fluctuations in engine geometries.

3.1. Hybrid spatial scheme

Travin et al. (2002) suggested a blending function for the inviscid fluxes $F_{inviscid}$:

$$F_{inviscid} = (1 - \sigma)\cdot F_{central} + \sigma \cdot F_{upwind}. \tag{18}$$

The blending function σ guarantees upwind-based spatial differencing in the RANS region and central differencing in the LES region. The function reads as follows:

$$\sigma = \sigma_{max}\cdot \tanh(A^{*C_{H1}}) \tag{19}$$

with

$$A^* = C_{H2}\cdot max\left\{\frac{C_{\mathrm{DES}}\Delta/l_{turb}}{g^*} - 0.5, 0\right\}. \tag{20}$$

$$l_{turb} = \frac{\sqrt{k}}{C_\mu\omega} \tag{21}$$

The parameter g^* ensures upwind differencing in the disturbed irrotational flow regions where $\overline{\Omega} \ll 1$ and $\bar{S} > 0$. It is defined as

$$g^* = max\left(tanh\left[\left(\frac{C_{H3}\cdot\overline{\Omega}\cdot max\{\bar{S}, \overline{\Omega}\}}{max\{(\bar{S}^2 + \overline{\Omega}^2)/2, 10^{-10}\}}\right)^4\right], 10^{-10}\right). \tag{22}$$

The constants $C_{H1},\ C_{H2},\ C_{H3}$ and σ_{max} are given in Strelets (2001). In order to ensure consistency with the zonal restriction from Eq. (17), the final value of the blending function, denoted as σ^* in the following, is defined as

$$\sigma^* = max(\sigma, F_{\mathrm{SST}}), \tag{23}$$

where $F_{\mathrm{SST}} = F_1$ is used in our simulations

We consider three different spatial discretisation schemes available in the CFD solver CFX to be used with the hybrid scheme, namely a standard upwind (UD), a central differencing (CD) as well as a bounded second order upwind biased discretisation scheme called high resolution scheme (HR), respectively. The latter is based on a numerical advection corrector, which can be viewed as an anti-diffusive flux added to the upwind scheme. The flux is adapted according to the suggestion of Barth and Jesperson (1989) without violating boundedness principles.

A suitable test case is used to evaluate the level of numerical dissipation introduced by the numerical scheme. Homogeneous isotropic turbulence is initialized in a cubical computational domain and is simulated using Euler's equations. From a Reynolds-averaging point of view, the mean kinetic energy $\overline{K} = 1/2\bar{u}_k\bar{u}_k$ equals zero and only the fluctuating components of the velocity with the turbulent kinetic energy k are computed. Physically, the kinetic energy should stay constant over time in this test case.

The cubical domain considered has an edge length of $L = 3.2$ cm. The grid consists of 32^3 hexahedral elements with an homogeneous grid spacing. Periodic boundary conditions are used for all faces and the time step Δt is based on an acoustic CFL-number of $\mathrm{CFL}_a = 0.6$. The turbulent velocity field is initialized using a 3D spatial inverse Fourier-transformation of a von Kármán–Pao type energy spectrum.

In Fig. 1 the level of numerical dissipation is quantified as a function of time. The CD scheme introduces the lowest amount

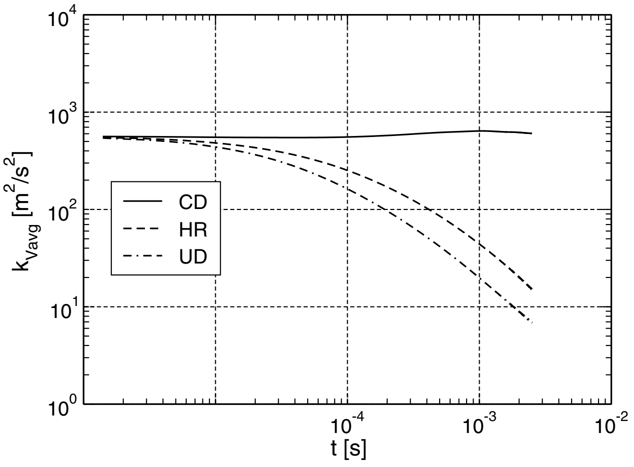

Fig. 1. History of volume-averaged kinetic energy k_{Vavg} for several spatial schemes.

of numerical dissipation followed by the HR scheme. As expected the UD scheme yields the largest amount of numerical dissipation leading to a rapid decrease of kinetic energy. According to these results the CD and HR scheme are used for the formulation of the fluxes in Eq. (18). The HR scheme is chosen for the SST URANS computations.

3.2. Determination of C_{DES}

Decaying isotropic turbulence can be used for the evaluation of SGS models. In order to calibrate the factor C_{DES} in Eq. (17) simulation results are compared to wind tunnel experiments of Comte-Bellot and Corrsin (1971), which can be transferred to decaying homogeneous and isotropic turbulence in a box by means of the hypothesis of Taylor (1935). It is important to note that both the $k-\varepsilon$ and the $k-\omega$ branches exist in the SST-based SGS model and the corresponding C_{DES} value should be calibrated independently for either branch according to Travin et al. (2002). The final value of C_{DES} is blended according to

$$C_{\mathrm{DES}} = (1 - F_1)C_{\mathrm{DES}}^{k-\varepsilon} + F_1 C_{\mathrm{DES}}^{k-\omega}. \tag{24}$$

Considering that the LES mode of the SST-based DES is mostly active away from the wall, the $k-\varepsilon$ branch will be dominant and we will investigate C_{DES} for the $k-\varepsilon$ branch first.

The turbulent Reynolds number based on the Taylor scale of the original experiment is about $Re_\lambda = 70$. Three-dimensional energy spectra were measured at three different locations behind the grid at $\frac{tU_0}{M} = 42$, 98 and 171, which correspond to three different times during the decay of turbulence in a box, respectively. The computation is performed for atmospheric pressure and temperature. Three cubical meshes with different grid resolutions and an edge length of $L = 0.508$ m are used. The grids consist of 32^3, 64^3 and 90^3 hexahedral elements with an homogeneous grid spacing. Periodic boundary conditions are used on all faces. The velocity field is initialized by means of a 3D spatial inverse Fourier-transformation of the energy spectrum $E(\kappa)$ in wavenumber space, which were measured at the first location behind the grid at $\frac{tU_0}{M} = 42$.

Several calculations were carried out on these grids. Using $C_{\mathrm{DES}}^{k-\varepsilon} = 0.61$ showed consistent results for the resolved scales on all grids and a good prediction of the turbulence decay over time. Thus, this value is used in the remainder of this study. Fig. 2 shows an example for the 64^3 grid resolution. Comparable results were obtained with the Smagorinsky model using $C_S = 0.2$. It is interesting to note the value for $C_{\mathrm{DES}}^{k-\varepsilon} = 0.61$ agrees with the finding of Travin et al. (2002). They also determined $C_{\mathrm{DES}}^{k-\omega} = 0.78$ to be a suitable value for the $k-\omega$ branch. As our value for $C_{\mathrm{DES}}^{k-\varepsilon}$ matches their va-

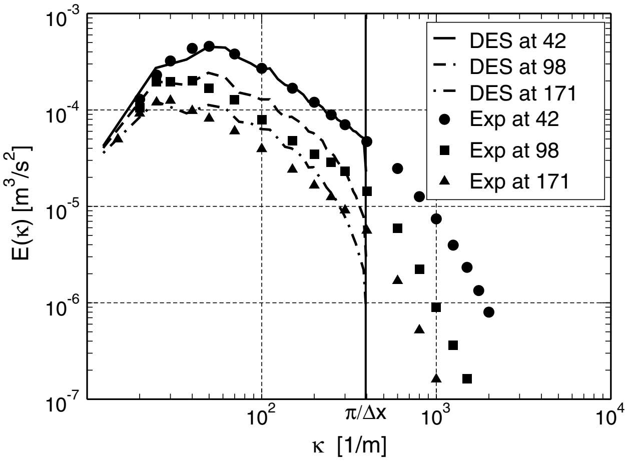

Fig. 2. Comparison of energy spectra of experiment and DES simulation at different times for 64^3 cells.

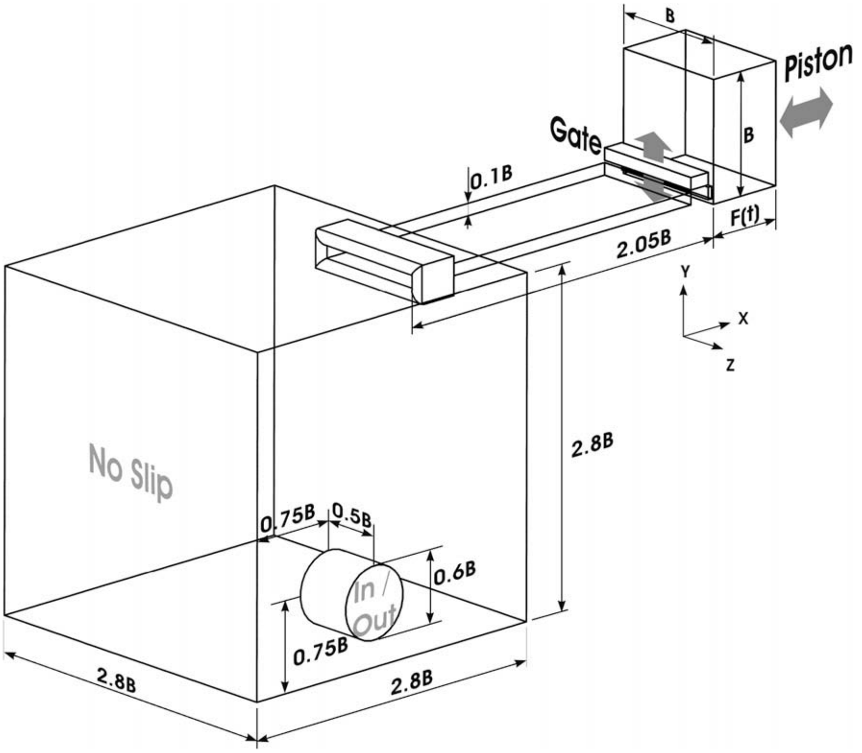

Fig. 3. Computational domain consisting of the cylinder, the intake channel and a large plenum (from right to left). Depending on the gate position, the intake channel and the cylinder are connected or disconnected. The essential dimensions and boundary conditions are included. B denotes the edge length of the square piston with $B = 10$ cm. $F(t)$ is a function of the piston lift.

lue, we decided to use their value for $C_{\mathrm{DES}}^{k-\omega} = 0.78$ for the blending function given in Eq. (24).

4. Cyclic variations in a simplified engine setup

Boreé et al. (2002) studied the generation, compression and breakdown of a tumbling motion experimentally in an engine-type setup. Two-dimensional PIV measurements of 100 consecutive cycles at various crank angle positions are available for the symmetry plane of the chamber and are used for comparison with the simulation throughout this investigation. A large scale vortex in an IC-engine is referred to as tumble if the axis of the rotational motion is perpendicular to the cylinder axis. This flow type is of increasing importance for modern turbo-charged, direct-injection gasoline engines, where it has a major influence on the intake manifold design. The tumble is generated during the intake stroke. The large scale motion becomes unstable during compression as the piston rises towards TDC and breaks down to smaller scales.

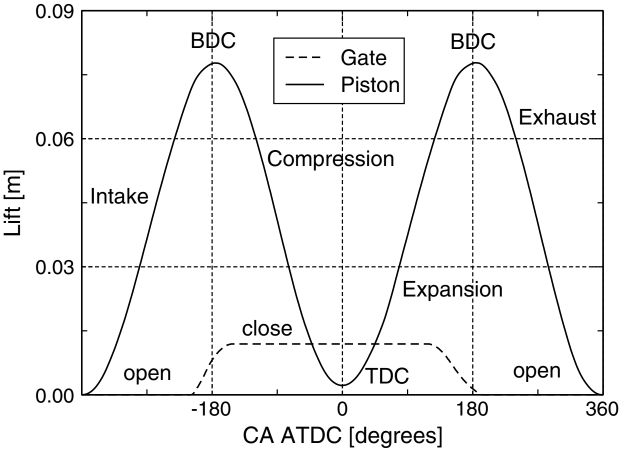

Fig. 4. Gate and piston lift over crank angle.

In the experiment, air enters and leaves the compression chamber via a rectangular channel that can be opened and closed by a gate device, which is used instead of engine valves. A plenum is located upstream of the intake channel in order to prepare seeding for the PIV measurements. Due to the square-shaped cross-section of the chamber, the square piston and the usage of a simple gate, the tumbling motion is better defined in the experiment of Boreé et al. (2002) than in a real IC-engine where the geometry is much more complex. The model compression machine allows easier reproducibility of the boundary conditions in simulations and good optical access. The compression ratio is 4 and the resulting peak pressure is $p_{max} = 5.5$ bar. The length to height ratio of the intake channel ($L/h = 30$) guarantees that turbulence is fully established when the flow reaches the chamber. During the intake stroke the maximum Reynolds number based on the hydraulic diameter is $Re_{max} = 12000$.

4.1. Numerical setup

Fig. 3 sketches the basic dimensions of the computational domain, which consists of the cylinder, the intake channel and a large plenum. The plenum has a pipe connecting it with the atmosphere. Depending on the piston movement both inflow and outflow can happen at this interface. For subsonic inflow to the boundary, the outside total pressure and temperature are prescribed. In addition, the direction of the velocity vector is specified as normal to the inlet. For subsonic outflow, the static pressure is specified at the integration points. For the velocities, the convective fluxes at the boundary integration points are computed using interior nodes only (upwind values). The diffusive fluxes are set to zero. For all other boundaries no-slip conditions are used. For the aluminum piston a constant temperature of $T_{piston} = 22.5\,^{\circ}\mathrm{C}$ was measured on the surface, and this value was used in the simulation. For the optical access large parts of the chamber side walls (liner), which

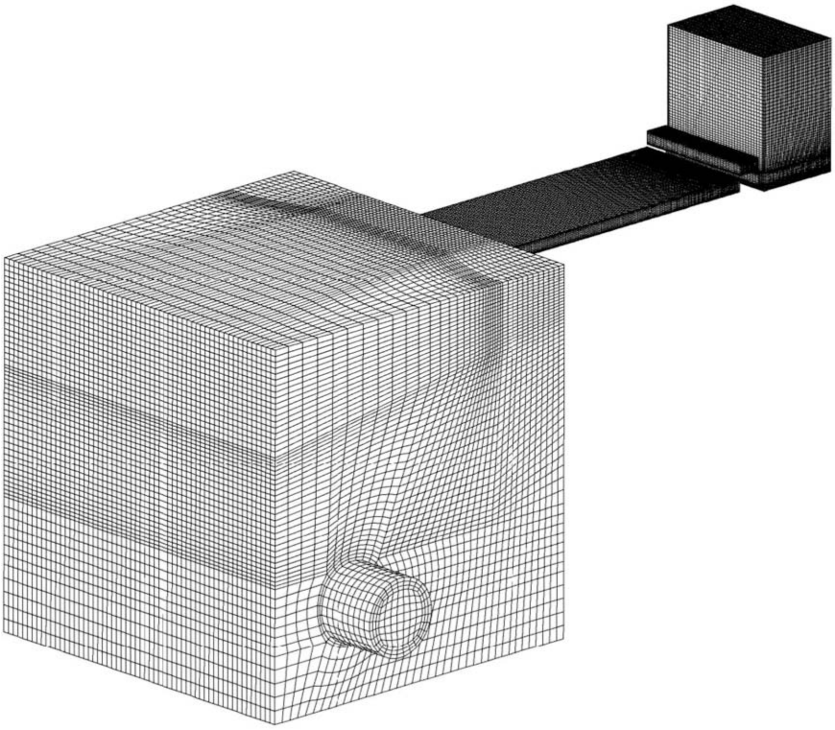

Fig. 5. Computational mesh.

are in contact with the piston, and the cylinder head are thick windows. Since the conductivity of the windows is low and only free convection can take place at the outer walls, the liner and the cylinder head are assumed to be adiabatic. According to the measurements the temperature of the other walls of the experimental setup is constant at $T_{wall} = 18.8\,^{\circ}\mathrm{C}$. The time step is $\Delta t = 2 \cdot 10^{-4} s = 0.2472^{\circ}$ CA. The highest CFL-numbers occur during the intake stroke due to the high jet velocities. An analysis for the flow field at 240° CA bTDC as shown in Fig. 8 yields that $\mathrm{CFL} < 1$ is valid for 85% and $\mathrm{CFL} < 1.5$ is valid in 96% of all cells. The maximum CFL number is smaller than 3. During most of the cycle the velocities are significantly smaller and $\mathrm{CFL} < 1$ is valid in the whole domain.

The gate and the piston lift are depicted in Fig. 4. The end of compression stroke is at 0° crank angle (CA), the corresponding piston position is referred to as Top Dead Center (TDC) and the volume of the chamber is at minimum. In the following we will describe piston positions in crank angle relative to TDC, meaning that 240° CA before TDC (bTDC) is identical -240° CA in Fig. 4. 180° CA is Bottom Dead Center (BDC) and the volume of the chamber is at maximum.

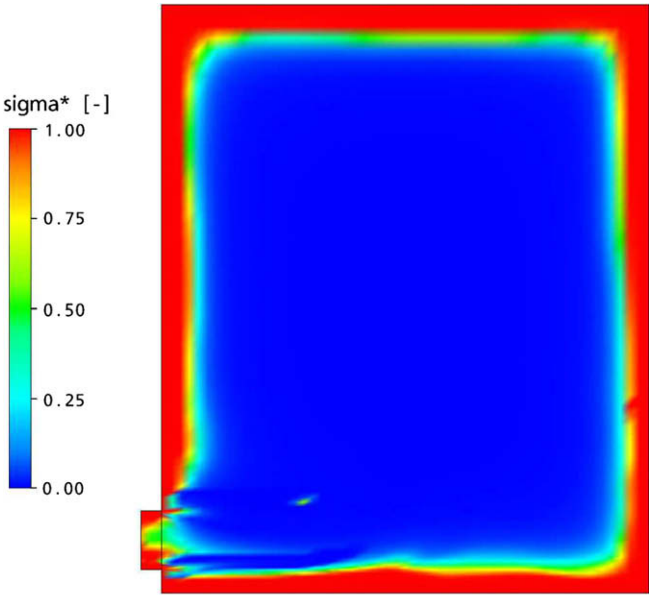

Fig. 6. Instantaneous field of the blending function σ^* for the hybrid spatial scheme at 240° CA bTDC.

Fig. 5 outlines the computational mesh, which consists of 391551 nodes. Due to the simple geometry of the chamber, the complete grid movement can be managed with only one computational mesh, which is deformed according to the valve and the piston lift.

For the URANS simulation a single cycle is computed for initialization. The results shown below were taken from the following cycle. Continuation of the URANS calculation showed only small differences. The DES was started using the results of the URANS calculation as initial solution. In order to minimize the impact of the initial solution 4 complete DES cycles were computed. The DES was carried out for additional 10 cycles and these results for single and phase-averaged (not using the first four cycles) fields are discussed below. The issue of statistic reliability is specially addressed at the end of Section 4.2 by a comparison of the results based on 10 computational cycles with those of 100 experimental ones.

An important requirement for DES to predict cyclic fluctuations is that the focus region must have an adequately fine grid resolution such that LES is used there.

Fig. 6 shows the blending function σ^* of the hybrid scheme, see Eq. (18), for 240° CA (and is comparable for other crank angles). While σ^* is not an exact indicator of the LES region, it gives a good indication of the region, where both, model formulation and numerical treatment, switch to LES-mode. It can be seen that the complete inner part of the chamber is indicated as an LES-zone.

The isosurfaces of $S^2 - \Omega^2 = 500 s^{-2}$ at 240° CA bTDC for both the DES and the URANS computation are shown in Fig. 7, visually demonstrating the different levels of turbulence resolution.

Using the subgrid kinetic energy computed by the LES, a rough estimate of the resolved fluctuations can be made. For the same crank angle as in Figs. 6–9 we used 10 DES cycles to compute the fluctuating components u', v' and w' in the LES focus region by subtracting the averaged field. The resolved part of the turbulent energy is then computed by

$$X_{res} = \frac{0.5(u'^2 + v'^2 + w'^2)}{k_{SGS} + 0.5(u'^2 + v'^2 + w'^2)}. \tag{25}$$

For all cycles values between 84% and 91% are obtained for X_{res}, the average value is 88%.

4.2. Results

The analysis of the results is divided into two major parts. First, we compare the general flow structure from DES and experiment and then detailed comparisons are presented of the predicted flow fields with experimental and available LES data for three different

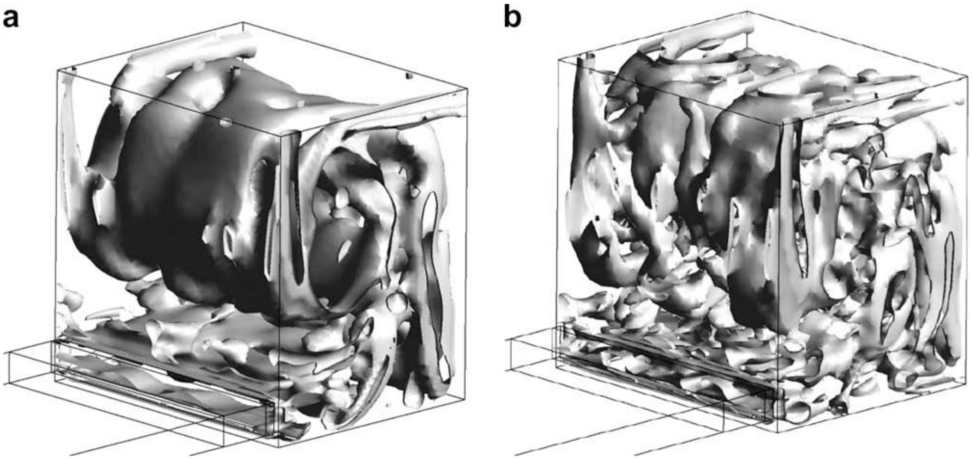

Fig. 7. Isosurfaces of $S^2 - \Omega^2 = 500\ \mathrm{s}^{-2}$ at 240° CA bTDC for (a) the SST URANS simulation and (b) the SST DES.

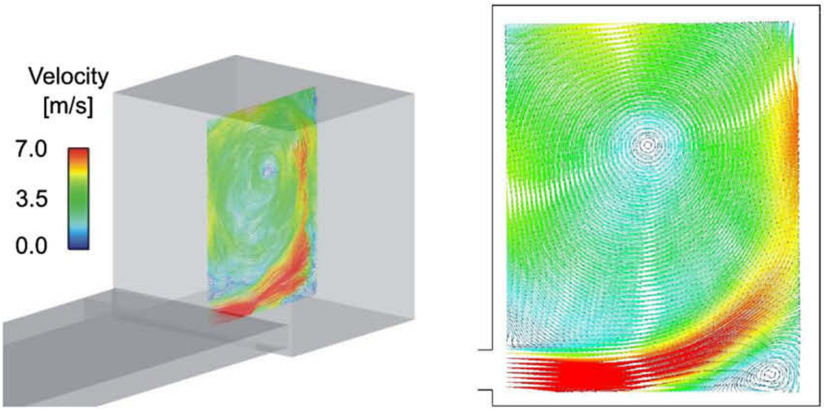

(a) Legendand Location of Measurement (b) Ensemble-Average

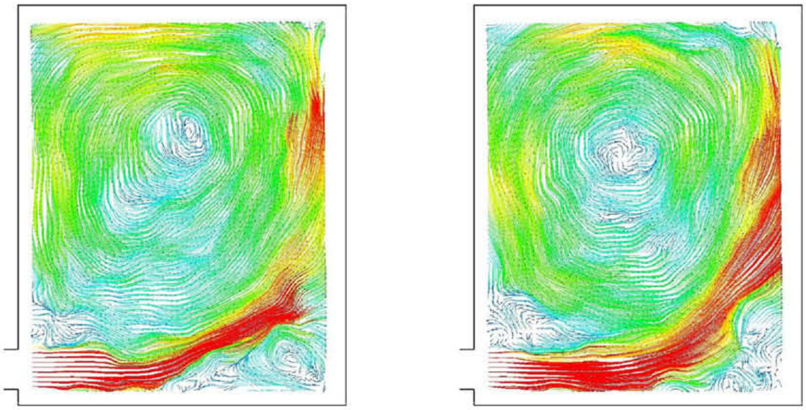

(c) Cycle 1 (d) Cycle 2

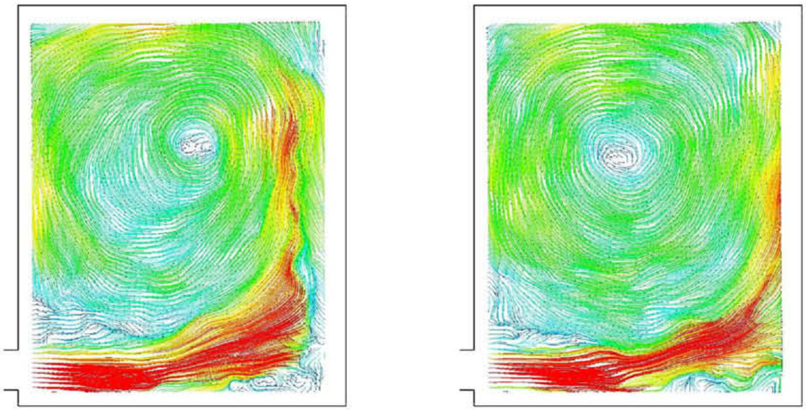

(e) Cycle 3 (f) Cycle 4

Fig. 8. Experimental phase-averaged velocity field of 100 cycles and instantaneous velocity fields of four consecutive cycles during the intake stroke at 240° CA bTDC.

crank angles. We also cover the aspect of statistical convergence with respect to the number of simulated cycles.

Figs. 8 and 9 show the phase-averaged and the instantaneous velocity fields at the same crank angle 240° CA bTDC during the creation of the tumble in the intake stroke of the experiment and the DES, respectively. In the experiment the phase-average is determined over 100 cycles whereas in the simulation 10 cycles are considered. To provide a first impression of the cycle to cycle differences in the flow field, the instantaneous velocity fields are given for 4 consecutive cycles for both the simulation and the experiment. Comparing the averaged fields, the recirculation bubble in the lower right corner, which results from the reflection of the jet on the piston surface, is more pronounced in the simulation compared to the experiment. This results from flow fields as they occur e.g. in cycle 2 depicted in Fig. 9d. This effect might be less pronounced if more than 10 cycles were available for the phase-averaging. Significant variations from cycle to cycle in the size of the recirculation zone can also be seen in the experimental data, see e.g. cycles 1 and 3 in Fig. 8c and e. However, there are only a few cycles with such large recirculation zones as for cycle 1 and this flow structure averages out over the 100 cycles, which might explain the differences between the predicted and experimental averaged fields. A large vortex slightly above the

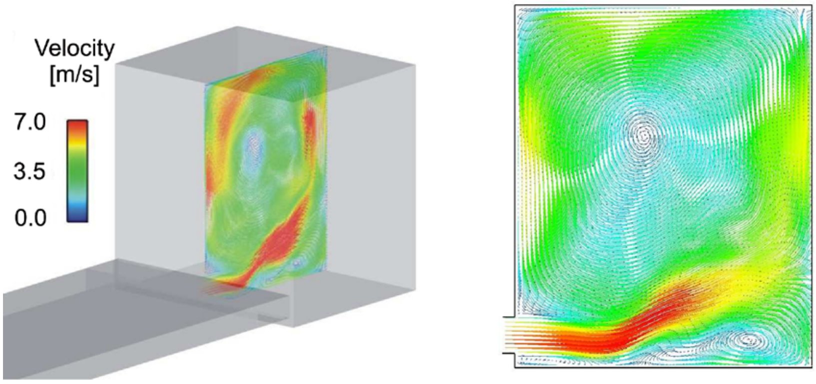

(a) Legend and Location of Cross Section (b) Ensemble-Average

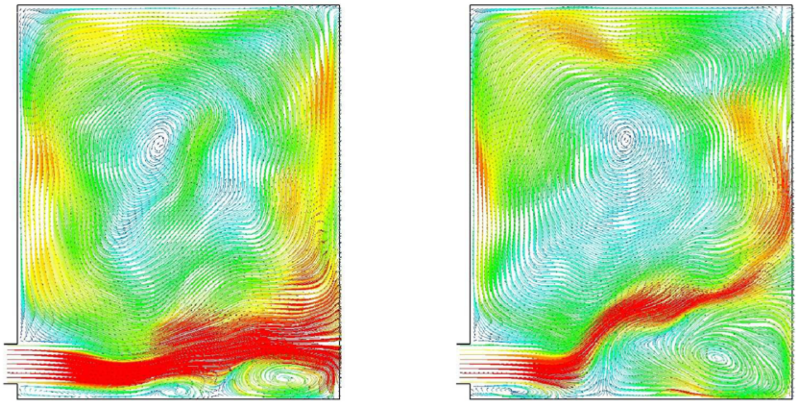

(c) Cycle 1 (d) Cycle 2

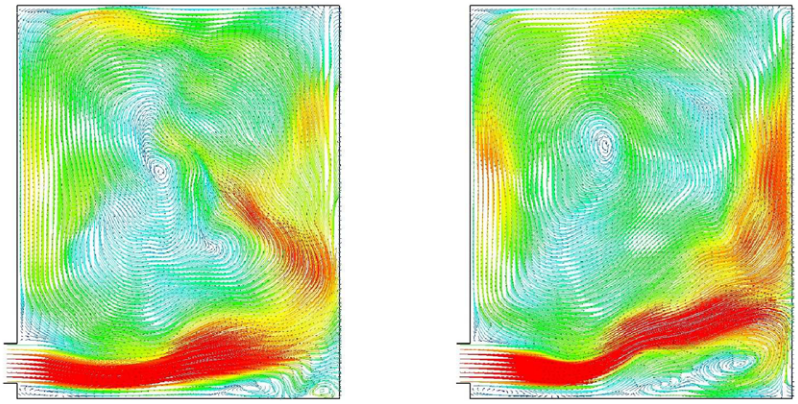

(e) Cycle 3 (f) Cycle 4

Fig. 9. DES result for the phase-averaged velocity field of 10 cycles and for instantaneous velocity fields of four consecutive cycles during the intake stroke at 240° CA bTDC.

center can be observed in both the experiment and the simulation. Its position changes from cycle to cycle and this precessing motion is further discussed below in detail.

Fig. 10 shows the instantaneous z-component of vorticity in the symmetry plane during the intake and compression stroke. Two mixing layers and counter-rotating vortices, see the discussion above, developing from the edges of the intake can be observed. These vortices are deflected by the piston. A shear layer on the piston is visible and a large scale tumble with positive vorticity develops due to spiral roll-up. This wall-vortex interaction in a confined environment is expected to have an impact on the large scale precession already seen in Figs. 8 and 9.

In Figs. 11–13, we compare results of DES and URANS obtained in the present work for three different crank angle/piston positions, namely, 270° CA bTDC, 90° CA bTDC and TDC, with the experimental data and with the LES of Moureau et al. (2004). For the latter, only the averaged velocities are available. The exact location of the comparison of the one-dimensional profiles is sketched in subfigure (a). Instantaneous velocity profiles of six consecutive cycles from the DES and the experiment are included in subfigures (b), (c), (f), (g), which is an indication of the resolved cycle to cycle fluctuations. The phase-averaged values are based on 10 consecutive cycles in the DES and 100 cycles in the experiment. For the URANS simulation a single cycle is used for comparison. The LES results by Moureau et al. (2004) are based on six computed LES cycles.

Fig. 11 shows the results for 270° CA bTDC, which is halfway during the intake stroke. The phase-averaged u-velocity profile of the DES (c) agrees fairly well with the experiment (b) and is very

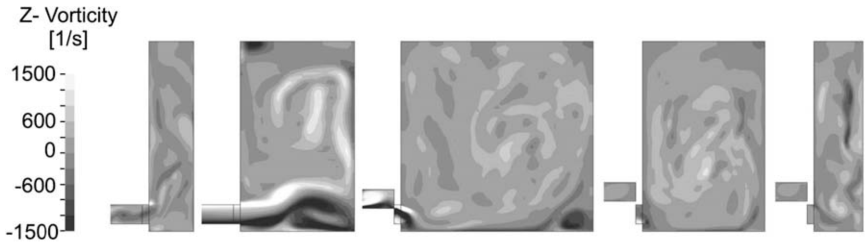

Fig. 10. DES result of *z*-component vorticity during intake and compression stroke.

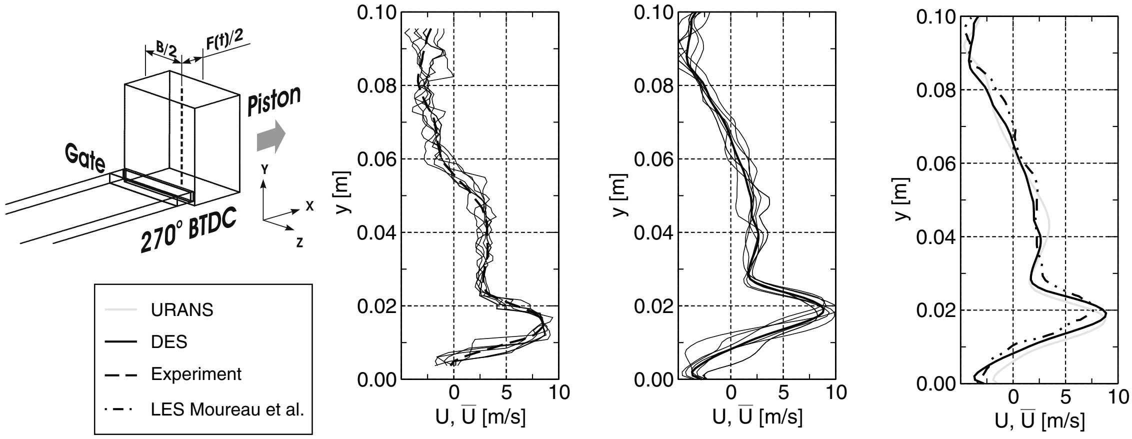

(a) Legend/Sketch (b) Experiment (c) DES (d) URANS/DES/LES

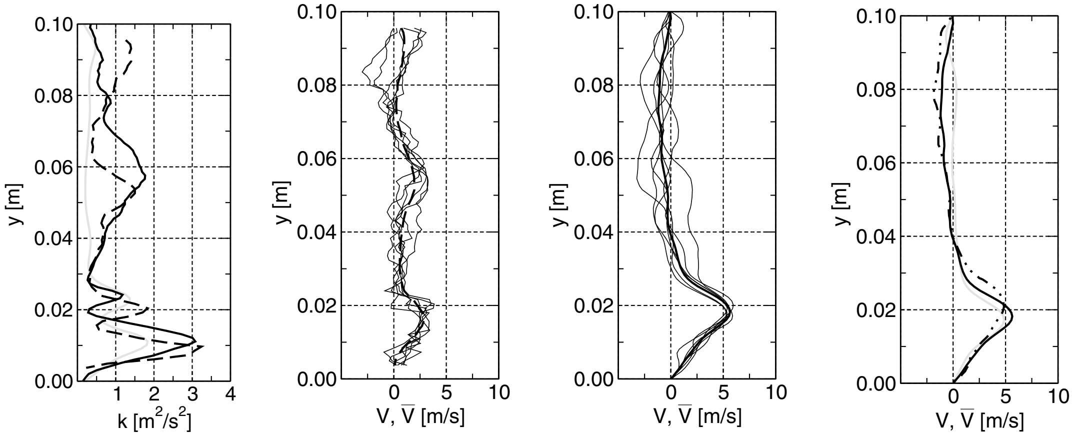

(e) URANS,DES, Experiment (f) Experiment (g) DES (h) URANS/DES/LES

Fig. 11. (a) shows the location (dashed line) for the comparison of simulation and experiment at 270° CA bTDC. (b)–(d) compare the averaged *u*-velocity component of the experiment, DES, URANS and the LES calculation by Moureau et al. (2004). The instantaneous *u*-velocity profiles for six consecutive cycles (thin) and the averaged profiles (thick) are given for the experiment and the DES in (b) and (c), respectively. (f)–(h) show the same configuration for the *v*-velocity component. The comparison of the two-dimensional turbulent kinetic energy $k = \frac{1}{2}\cdot(\bar{u}'^2 + \bar{v}'^2)$ of DES and URANS with experiment is presented in (e). For URANS the two-dimensional turbulent kinetic energy is calculated under the assumption of isotropy as $k = \frac{2}{3}k_{modelled}$.

similar to the profile of the URANS simulation and the LES results (d). As expected from theory the comparison of the instantaneous profiles shows that the wiggles in the DES (c) are smoother than in the experiment (b) since the small turbulent structures are modelled and not resolved. Neither the DES simulation (g) nor the URANS/LES results (h) show the peak of the averaged *v*-velocity profile in the middle of the chamber, which can be observed in the experiment (f). This is due to the fact that the locations of the vortex core in the simulation and the experiment slightly differ. The two peaks of the two-dimensional turbulent kinetic energy (e) in the lower half of the chamber $y < 0.03$ m are caused by turbulent production in the shear layers. The URANS simulation underpredicts the kinetic energy in that region. Since the size of the recirculation bubble of the entering flow is overpredicted as observed in the two-dimensional velocity field in Fig. 9b for a later crank angle, the peaks of the turbulent kinetic energy (e) and the averaged *u*- (c) and *v*-velocity (g) profiles in the lower region are slightly shifted in positive *y*-direction, which can be seen for all simulation results. A peak of the turbulent kinetic energy can be observed in the middle of the chamber, which is close to the center of the large tumble core, in the experimental data and the DES results. Boreé et al. (2002) performed proper orthogonal decomposi-

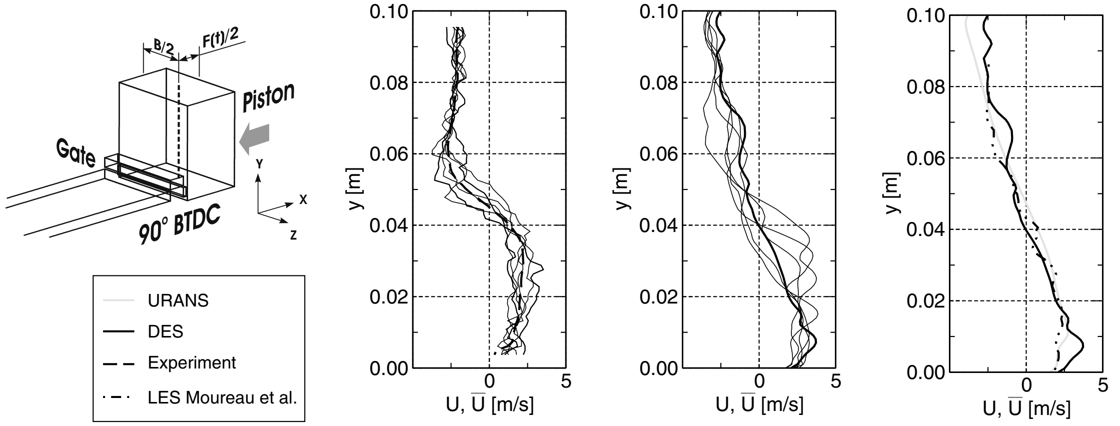

(a) Legend/Sketch (b) Experiment (c) DES (d) URANS/DES/LES

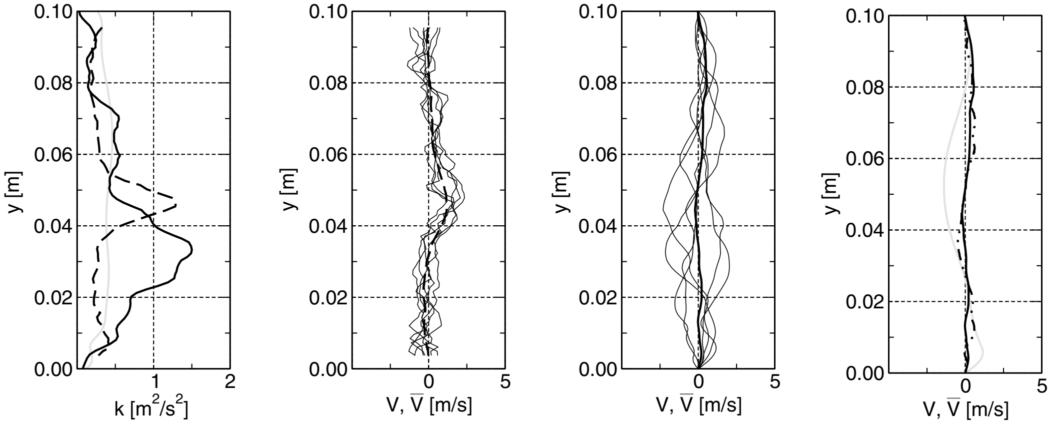

(e) URANS, DES, Experiment (f) Experiment (g) DES (h) URANS/DES/LES

Fig. 12. Same as is in Fig. 11 for 90° CA bTDC.

tion (POD) of that central region of the tumble and they could clearly show that an important contribution to the phase-averaged turbulence in that region is due to the large scale displacements of the vortex, an effect that as shown by Haworth (1999) can be directly linked to cycle to cycle fluctuations in the context of engine applications. While the DES captures that phenomenon, the URANS simulation shows a constant level of turbulent kinetic energy in that region. Production of turbulent kinetic energy in shear layers is reasonably well predicted by URANS whereas turbulence due to cyclic flow variations cannot be detected. This is consistent with the results shown in Fig. 11e, where the overall resolved kinetic energy of the DES is shown to be comparable to the experimental values. It is important to note that the averaged velocity field from the URANS simulation is comparable to both DES and LES results at this crank angle position. However, the peaks of turbulent kinetic energy due to both shear and large scale cyclic flow variations are captured in the DES and compare reasonably well with the experimental data. These findings are in agreement with the results of Toledo et al. (2007). Le Roy and Le Penven (1998) also showed for a similar flow configuration as this one that the RANS approach predicts a minimum of turbulent kinetic energy in the center of the tumble motion.

The results of the simulation and the experiment at 90° CA bTDC during compression are presented in Fig. 12. Although in the experiment (b) the S-shape of the profile is more pronounced, the averaged u-velocity profile is reasonably well predicted by the URANS simulation, the LES (d) as well as the DES (c). The averaged v-velocity profiles of the DES and LES (h), (g) and the experiment (f) also agree reasonably well. However, the URANS simulation (h) shows negative values for the averaged v-velocity component in the middle of the cylinder, which indicates that the location of the vortex core differs from the experiment. Similar to the intake stroke the peak of the turbulent kinetic energy in the middle of the cylinder (e) can be captured by the DES. However, the location is shifted in negative y-direction compared to the experiment. This is due to the different positions of the precessing vortex core from cycle to cycle as it was discussed above. An indicator of the averaged deviation is the difference of the location where the instantaneous u-velocity profiles equals zero. In both the experiment and the DES the position varies by roughly 1 cm. The URANS simulation shows a constant level of turbulent kinetic energy almost over the complete cross-section, as it cannot capture the large scale cyclic fluctuations, which correspond to the first POD modes as determined by Boreé et al. (2002).

Finally, the results at the end of compression at TDC are depicted in Fig. 13. The averaged u-velocity profile of the experiment (b) still shows a slight S-shape, which cannot be observed in the DES (c), the LES and the URANS simulation (d). The v-velocity profile is well predicted by the DES (g) and the LES (h). However, the result of the URANS simulation (h) essentially differs from the experiment in the middle of the cylinder, which is comparable to the finding for 90° CA bTDC. In the URANS simulation almost no turbulent kinetic energy can be observed at TDC (e). The level of the turbulent kinetic energy in the DES is signifi-

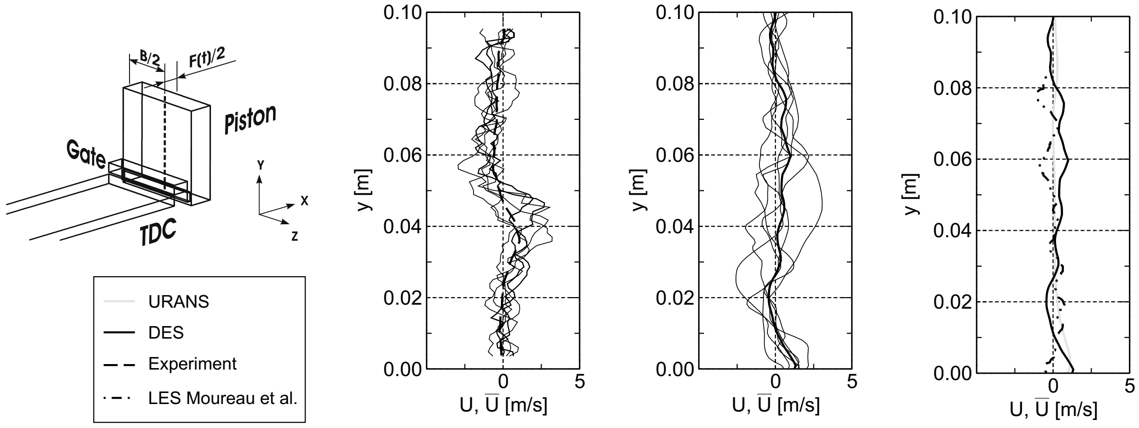

(a) Legend/Sketch (b) Experiment (c) DES (d) URANS/DES/LES

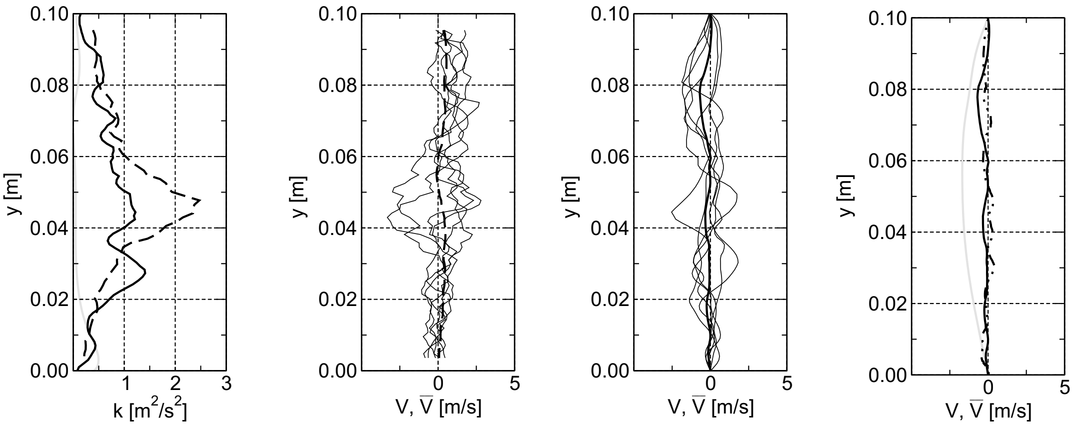

(e) URANS, DES, Experiment (f) Experiment (g) DES (h) URANS/DES/LES

Fig. 13. Same as is in Fig. 11 for TDC.

cantly higher but still lower than the experimental value. However, the peak, which is still very pronounced in the experiment and is present in the DES at earlier crank angles, cannot be observed anymore.

As mentioned above the experimental data was averaged for 100 cycles whereas the DES results were obtained from 10 consecutive cycles, which is comparable to Moureau et al. (2004) with six LES cycles and Toledo et al. (2007) with 10 LES cycles. However, this raises the issue whether 10 cycles are sufficient for reliable statistics. It can be concluded from Figs. 11–13 that the agreement between the experiment and DES results for the mean velocity and the turbulent kinetic energy is satisfactory initially but declines during the compression. Flow visualizations from either experiment or simulation for the different cycles show that during the intake stroke the flow is essentially two-dimensional, variations are mainly due to the precessing vortex core and fluctuations of the jet impact zone. The number of computed cycles appears to be sufficient for a reliable description of that phase. However, during compression the symmetry is lost and the fluctuations are amplified through transfer of energy from the mean flow. Consequently the mean flow becomes weaker and increasing differences between each realization are observed for both experiment and DES. Thus, statistical convergence is expected to become slower for later stages of the compression and the differences at TDC in Fig. 13 support that statement. The agreement is expected to improve for an increased number of simulated cycles. A similar conclusion can be drawn for the simulated size of lower recirculation zone in Fig. 9 and the position of the precessing vortex core.

5. Summary

Cyclic variations of the fluid flow are an important aspect in today's engine design and optimization process, as they have a significant influence on the combustion and therefore on the overall engine performance. They usually cannot be resolved using RANS-based modelling approaches. The present study investigated the feasibility of using the SST DES and SST URANS models to predict cycle to cycle variations in a geometrically simplified internal combustion engine. If the grid resolution is sufficiently fine, an LES model is used in the inner part of the domain, which is usually the region of intense shear flow. For regions, where the grid resolution is not sufficient for LES as well as in the near-wall regions, the URANS SST model is used. For LES, the issue of numerical dissipation is especially important and this aspect was covered in Section 3 showing that the chosen numerical scheme is suited for this type of application.

It was shown that the focus region is simulated using LES, with up to 80–90% of the turbulent kinetic energy during the intake stroke being resolved, which is a prerequisite for the prediction of cyclic fluctuations. Turbulent statistics of the models and the measured velocity field are compared to assess the capability of DES to predict cyclic variations. During the intake stroke the computed phase-averaged velocity fields for both URANS and DES give good agreement with the experiment. The turbulent kinetic energy shows three distinct peaks, two of them can be linked to the production in the shear layers at the upper and lower connection of the intake channel. These two peaks are predicted by both the

DES and the URANS results, however with better results for the DES and the URANS peak being lower due to the higher level of the eddy viscosity. Using POD Boreé et al. (2002) showed that the third peak is due to the precessing large scale motion of the tumble core. This large scale fluctuation can be directly linked to cyclic variability in engines, see e.g. Haworth (1999). This fluctuation is captured only by the DES, which is a very encouraging result concerning the prediction of cycle to cycle variations in complex engine geometries. During the compression stroke the predicted averaged velocity field of the DES is more realistic than the URANS simulation and agrees reasonably well with the experiment, however the agreement during intake stroke is better than during the compression stroke. The increasing variability from one to the next realization shows that an increased number of cycle simulations is likely to improve the statistics especially during the compression stroke.

Acknowledgements

The authors would like to thank Florian Menter for helpful discussions. The authors also acknowledge the detailed comments and suggestions from the reviewers. This work was partially financed the European Commission (LESSCO2 Project, Contract No. ENK6-CT-2002-00616).

References

Barth, T.J., Jesperson, D.C., 1989. The Design and Application of Upwind Schemes on Unstructured Meshes, AIAA Paper (89-0366).

Boreé, J., Maurel, S., Bazile, R., 2002. Disruption of a compressed vortex. Phys. Fluids 14 (7), 2543–2556.

Boussinesq, J., 1877. Essai sur la theorie des eaux courantes. Memoire present'ees par divers savantes a l'Academie des Sciences L'Institute de France, Paris 23 (1), 1–680.

Comte-Bellot, G., Corrsin, S., 1971. Simple Eulerian time correlation of full- and narrow-band velocity signals in grid-generated 'isotropic' turbulence. J. Fluid Mech. 48, 273–337.

Constantinescu, G.S., Squires, K.D., 2003. LES and DES investigations of turbulent flow over a sphere at Re = 10,000. Flow Turbulence Combustion 70, 267–298.

Haworth, D.C., 1999. Large eddy simulation of in-cylinder flows. Oil Gas Sci. Technol. 54, 175–185.

Jones, W.P., Launder, B.E., 1972. The prediction of laminarization with a two-equation model of turbulence. Int. J. Heat Mass Transfer 15, 301–314.

Launder, B.E., Sharma, B.I., 1974. Application of the energy-dissipation model of turbulence to the calculation of flow near a spinning disc. Lett. Heat Mass Transfer 1, 131–138.

Le Roy, O., Le Penven, L., 1998. Compression of a turbulent vortex flow. Int. J. Heat Fluid Flow 19, 533–540.

Menter, F.R., 1993. Zonal Two-equation $k-\omega$ Turbulence Models for Aerodynamic Flows, AIAA Paper (1993-2906).

Menter, F., 2008. Private Communication.

Moureau, V., Barton, I., Angelberger, C., Poinsot, T., 2004. Towards Large Eddy Simulation in Internal-Combustion Engines: Simulation of a Compressed Tumble Flow, SAE (2004-01-1995).

Spalart, P.R., Jou, W.-H., Strelets, M., Allmaras, R., 1997. Comments on the feasibility of LES for wings, and on a Hybrid RANS/LES approach. In: Liu, C., Liu, Z. (Eds.), 1st AFOSR Int. Conf. on DNS/LES 1997, Ruston, LA. In Advances in DNS/LES, Greyden Press, Columbus, OH.

Spalart, P.R., Deck, S., Shur, M.L., Squires, K.D., Strelets, M.Kh., Travin, A., 2006. A new version of detached-eddy-simulation, resistant to ambiguous grid densities. Theor. Comput. Fluid. Dyn. 20, 181–195.

Strelets, M., 2001. Detached Eddy Simulation of Massively Separated Flows, AIAA Paper (2001-0879).

Taylor, G.I., 1935. Statistical theory of turbulence. Proc. Roy. Soc A151, 421–478.

Toledo, M.S., Le Penven, L., Buffat, M., Cadiou, A., Padilla, Judith, 2007. Large eddy simulation of the generation and breakdown of a tumbling flow. Int. J. Heat Fluid Flow 28, 113–126.

Travin, A., Shur, M., Strelets, M., Spalart, P., 2000. Detached-eddy simulation past a circular cylinder. Flow Turbulence Combustion 63, 292–313.

Travin, A., Shur, M., Strelets, M., Spalart, P.R., 2002. Physical and numerical upgrades in the detached-eddy simulation of complex turbulent flux flows. Fluid dynamics and its applications. Advances in LES of complex flows. In: Friedrich, R., Rodi, W. (Eds.), Proc. of EUROMECH Colloquium 412, vol. 65. Kluwer Academic Publishers, Dordrecht/Boston/London, pp. 239–254.

Wilcox, D.C., 1993. Turbulence Modeling for CFD. DCW Industries.

Yan, J., Mockett, C., Thiele, F., 2005. Investigations of alternative length scale substitutions in detached-eddy simulation. Flow Turbulence Combustion 74, 85–102.